Controlled *in situ* growth of tunable plasmonic self-assembled nanoparticle arrays

2012 Nanotechnology 23 035606

(http://iopscience.iop.org/0957-4484/23/3/035606)

Nanotechnology **23** (2012) 035606 (9pp) doi:10.1088/0957-4484/23/3/035606

Controlled *in situ* growth of tunable plasmonic self-assembled nanoparticle arrays

R Verre, K Fleischer, J F McGilp, D Fox, G Behan, H Zhang and I V Shvets

Centre for Research on Adaptive Nanostructures and Nanodevices (CRANN) and School of Physics, Trinity College Dublin, Dublin 2, Ireland

E-mail: rverre@tcd.ie

Received 4 October 2011, in final form 7 November 2011
Published 16 December 2011
Online at stacks.iop.org/Nano/23/035606

Abstract

Self-assembled silver nanoparticle (NP) arrays were produced by deposition at glancing angles on transparent stepped Al_2O_3 templates. The evolution of the plasmonic resonances has been monitored using reflection anisotropy spectroscopy (RAS) during growth. It is demonstrated that the morphology of the array can be tailored by changing the template structure, resulting in a large tunability of the optical resonances. In order to extract detailed information on the origin of the measured dichroic response of the system, a model based on dipolar interactions has been developed and the effect of tarnishing and morphological dispersion addressed.

(Some figures may appear in colour only in the online journal)

1. Introduction

The reduced dimensions of noble metal nanoparticles (NPs) present unique characteristics which have been demonstrated to offer substantial advantages for different applications [1]. In particular, strongly coupled NPs below the diffraction limit provide an appealing resource as they can be used for waveguiding purposes [2–4], solar cell applications [5, 6] and biological analysis [7, 8]. The benefits of plasmonic systems with strong interparticle interaction have been confirmed in different research fields [9]. The presence of local electric field enhancement in the gap region of plasmon-coupled metal NPs is associated with enhancement effects, such as surface-enhanced Raman spectroscopy (SERS) [10], second-harmonic generation [11], fluorescence [12] and optical tweezers [13]. Potential application of these coupling effects is maximized by matching the structure resonances with the exciting laser for enhancement spectroscopy. Coupling has also been predicted to increase the sensitivity of refractive-index-based optical biosensors [14], and the stronger interaction results in an increase in the propagation distance of the optical excitations during waveguiding processes.

The progress in chemical synthesis of noble metal NPs from colloidal solutions has been dramatic in the last decade [15] and it is now possible to create particles of different dimensions and shapes, which facilitates a large tunability of spectral features and a variety of enhancement effects. Colloidal preparation, however, requires the dispersion of the nanocomposites onto a substrate, hence losing any long range order. Lithographic methods could offer a solution. However, giant enhancement effects require gaps between the NPs that are smaller than the average diameter which is difficult to achieve using current lithographic techniques [16]. In this paper an alternative and simple deposition method is used, where a collimated flux of adatoms is directed at a glancing angle of incidence towards a stepped surface in a high vacuum (HV) environment [17–19]. The self-assembly deposition technique produces highly ordered and strongly coupled NPs, well below the lithographic limit [20] and ordered on the macroscale (see figure 1). Glancing angle deposition readily presents itself as an alternative growth method capable of combining the large throughput required for any industrial application with the long range order normally attained for larger structures using lithography. Furthermore, unlike many other self-assembly

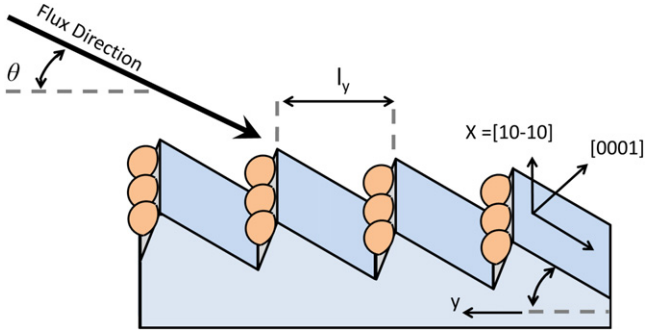

Figure 1. A schematic view of glancing angle deposition technique: a flux of collimated Ag adatoms is sent at a glancing angle of incidence θ towards a stepped surface. The substrate is an annealed *c*-plane Al_2O_3 miscut along the $[1\bar{2}10]$. The main crystallographic directions are indicated. The annealing produces a periodic structure of period l_y, consisting of steps (S) and terraces (T). After evaporation, the deposited material coalesces at the steps forming periodic NP arrays (average centre-to-centre distance l_x) coupled through electrostatic dipole forces [21]. The scale on the z axis has been exaggerated for clarity.

methods, it is a geometric deposition technique, virtually independent of the deposited materials.

In this paper we present a full investigation of the dependence of the Ag NP arrays on the initial template periodicity. It is first shown that different periodicities in the sub-100 nm range can be obtained by annealing *c*-plane Al_2O_3 substrates at different temperatures. The morphology of Ag NP arrays has been tailored by depositing at glancing angle on templates with different periodicities and the corresponding plasmonic properties have been tuned over a wide energy range, gaining the versatility of NP colloidal methods. To increase reproducibility, reflectance anisotropy spectroscopy (RAS) has been employed to monitor the resonant profiles during the growth *in situ*. It is demonstrated that highly tunable NP arrays possessing a precise resonant energy can then be obtained. Compared to previous works [18, 21], a full analytical model has also developed in this paper and the simulated spectra qualitatively reproduce the experimental results. In addition, the model elucidates the origin of the strong dichroic response of the sample, provides clear insights on the peak broadening of the spectra due to morphological dispersions and on the tarnishing effects of the outer layer due to exposure of the sample to the ambient atmosphere.

2. Growth and characterization of Ag NP arrays

The NP array layers have been produced in a two-step procedure, consisting of creating the stepped template and depositing Ag at a glancing angle. In order to obtain stepped templates, α-$Al_2O_3(0001)$ samples, off-cut 6° along the $[1\bar{2}10]$ direction, were annealed in atmosphere at temperatures from 1250 to 1450 °C. Figure 2 shows morphologies resulting after annealing at different temperatures. The surfaces form nearly periodic patterns, with a periodicity that can be tuned to below 100 nm [21]. Periodicities ranging from 30 to 150 nm are reported here and it can be seen that the average period increases exponentially with the annealing temperature (figure 2(D)). This effect is a consequence of a thermally activated diffusion process with an effective diffusion constant $D = D_0 \exp(-E_a/k_B T)$, where E_a is the activation energy. The linearity of the Arrhenius plot confirms this trend, showing that a change of annealing temperature is sufficient in producing different periodic arrangements. Similar periodic templates have also been produced on Si, amorphous Al_2O_3 or

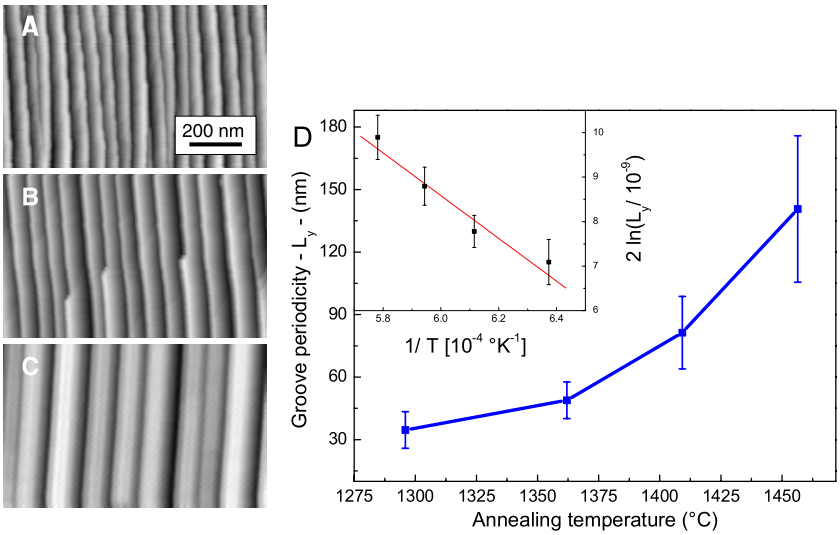

Figure 2. Faceting of *c*-plane Al_2O_3 miscut 6° along the $[1\bar{2}10]$ and annealed in ambient for 24 h. Annealing temperatures of 1360 °C, 1410 °C and 1460 °C produce periodic patterns with (A) 50 nm, (B) 80 nm and (C) 140 nm periodicity, respectively. Increases in the annealing temperature increase the periodicity exponentially (D). The linearity in the Arrhenius plot (inset) confirms the dominantly diffusion-activated process. In order to obtain a more reliable fit, a 32 nm periodic template, obtained by annealing at a temperature of 1296 °C, has also been produced.

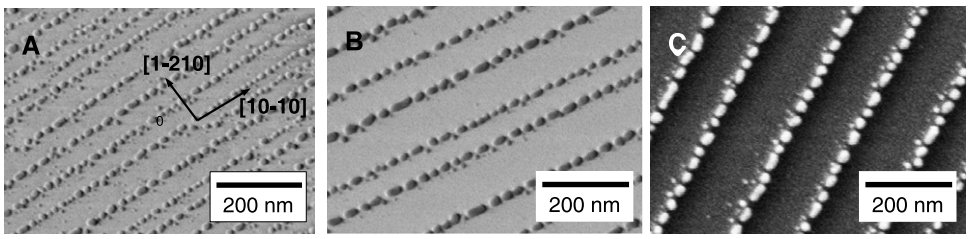

Figure 3. SEM images of the Ag NP arrays grown at glancing angle deposition for (A) 50 nm, (B) 80 nm and (C) 140 nm template periodicity.

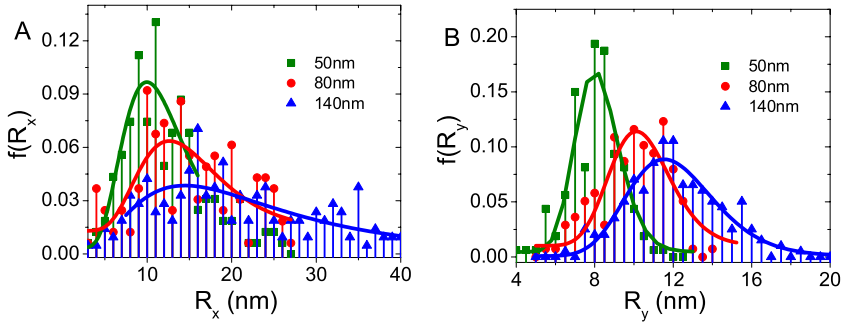

Figure 4. Frequency distribution of the in-plane semiaxes R_x (A) and R_y (B) for different template periodicities. Smaller periodicities result in smaller NPs and $R_y < R_x$ for a given periodicity. The log normal fits of the different distributions are indicated by the corresponding continuous lines.

even on glass substrates by means of Ar^+ ions sputtered at glancing angles [22, 23]. The simplicity of these techniques for forming the templates makes them attractive for possible industrial applications.

To grow Ag NPs, three substrates with 50, 80 and 140 nm periodicity were loaded at the same time into a UHV chamber and exposed for 30 min to a collimated Ag beam tilted at $\theta = 6°$ with respect to the average surface orientation. The angle was chosen in order to minimize the morphological dispersion [21]. Scanning electron microscopy (SEM) was used to characterize the NP morphology *ex situ* (see figure 3). The surface is covered by highly ordered clusters aligned along the facet edge and elongated along the chain axis. There are negligible numbers of NPs present in the middle of terraces. The phenomenon is attributed to a cluster growth mechanism with a diffusion barrier between step and terrace. Because of the glancing angle of deposition, adatoms land on the steps and then diffuse following a characteristic three-dimensional growth mode [24]. As the (0001) terraces have the lowest surface free energy configuration [25], the adatoms cannot overcome the diffusion barrier between step and terraces and all the material distributes on the facets as islands. The width of the NP chain and the separation between NPs are below the lithographic limit. The surface morphologies are remarkably uniform: the entire 5×5 mm^2 sample surface is covered by NPs of similar size and separation. The measured in-plane morphology is presented in table 1. As earlier, the indices x and y signify the in-plane directions along the chain of NPs and perpendicular to it, respectively. The interparticle separation much smaller than the average NP diameter ensures the strong coupling required for waveguiding purposes and for electric field enhancement.

For larger periodicity we observe an increase in the cluster anisotropy R_x/R_y and the average NP dimensions, and yet an almost constant interparticle separation. For a given Ag coverage, this can be explained in terms of nucleation sites determining the interparticle separation and centre-to-centre distance. Greater periodicities l_y produce larger facets and the initial adatoms nucleate further away from each other as a consequence of the longer diffusion length, resulting in larger centre-to-centre distances l_x. At the same time the lower facet density accompanying larger periodicities requires larger NPs to accommodate the same amount of deposited material, resulting then in an almost constant gap between the NPs. Furthermore, larger facets allow the lateral dimension of the NPs to increase. The morphology of the system, namely island anisotropy, interparticle distance and separation between the rows of NPs, can then be easily changed by simple modifications of both template annealing and NP deposition parameters.

The growth evolution has also been confirmed in figure 4 by the plot of the morphological frequency distribution of the NP semiaxes for the different templates. In particular, the confinement of the adatom diffusion perpendicular to the step results not only in $R_y < R_x$ but also in a much narrower distribution as the NPs are constrained within the facet. In contrast, along the facet edge, the NP shape is controlled mainly by diffusing mechanisms and the dispersion of the distribution is much larger, particularly for the large template periodicities. However, the order presented in this work is improved if compared with what was reported elsewhere utilizing similar growth methods [26, 23] and it is believed that depositions at higher temperature could further increase

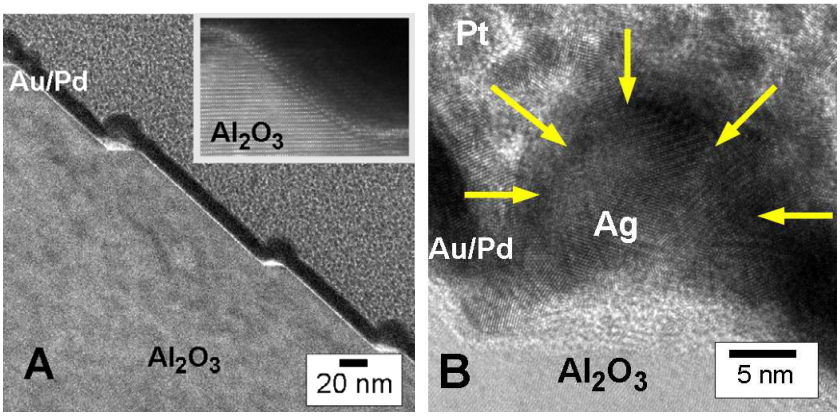

Figure 5. TEM section of a 80 nm periodicity substrate with Ag NPs deposited at glancing angle. (A) Low magnification and (B) high magnification. An Au/Pd layer was deposited by sputtering to protect the surface during the FIB section preparation. The arrows in (B) define the surface of the Ag NP. Inset of (A): substrate with similar periodicity before Ag deposition.

Table 1. Average interparticle centre-to-centre distance l_i, average separation along the axis, NP radii R_i and number of NPs per unit area N, obtained for templates with different periodicities after Ag glancing angle deposition. The statistics were obtained though analysis of the SEM images.

	50 nm	80 nm	140 nm
Ann. T. (°C)	1362	1410	1457
l_y (nm)	49 ± 9	81 ± 17	141 ± 35
l_x (nm)	23 ± 5	36 ± 8	42 ± 11
NP separation (nm)	6 ± 2	7 ± 2	5 ± 2
R_y (nm)	8.0 ± 1.3	10.0 ± 2.0	12.0 ± 2.3
R_x (nm)	8.6 ± 2.4	14.5 ± 3.5	18.4 ± 5.8
N ($\times 10^{14}$ part m^{-2})	8.9	3.4	1.7

the resulting morphology due to an exponential increase of the initial adatom diffusivity.

In order to obtain information on the out-of-plane morphology, sections of the array formed on the 80 nm periodicity template have also been produced using a focused ion beam (FIB) and investigated by transmission electron microscopy (TEM). A comparison of the array with a bare substrate of comparable step height is shown in the inset in figure 5. The height of the Ag NPs was determined to be $h = 13 \pm 4$ nm. Detailed examination of the images indicates that the Ag clusters are polycrystalline.

So far it has been demonstrated that the morphology of the NP layer can be tailored by glancing angle deposition on stepped templates with a periodicity that can be tuned, and consequent changes in the optical properties are expected. Nevertheless, accurate prediction of optical properties *a priori* remains difficult as the detail of the self-assembly process is not known. RAS measures the difference, at normal incidence, of the in-plane complex reflection coefficients r_i measured along two orthogonal directions, normalized to the overall reflection [27]:

$$\frac{\Delta r}{r} = 2\frac{r_x - r_y}{r_x + r_y}. \quad (1)$$

The great advantage of RAS is it provides a unique tool for monitoring the evolution of the optical behaviour of the anisotropic NP layer as it offers an *in situ* measurement capability.

Figure 6 shows the RAS spectra taken of the samples grown at growth interruptions and after exposure of the sample to the atmosphere. The bare substrate showed a negligible RAS signal of 2 units in the UV, confirming the overall in-plane optical isotropy of c-plane α-Al_2O_3. After Ag deposition, all samples showed double-peak features due to plasmon resonances. It has been shown previously that RAS and polarized transmission spectroscopy (PTS) provide equivalent information. In particular, the positive peak of the RAS reproduces the absorption profile when light is polarized along the array, while the negative peak reproduces the absorption peak for light polarized perpendicular to the array [21]. The peak heights increase with Ag coverage due to increased reflectance of the anisotropic layer and the peak positions undergo a redshift. The growth can then be interrupted in order to obtain a resonance at a particular energy, but subsequent exposure of the sample to the atmosphere changes the response due to tarnishing by sulfur adsorption. The optical change due to tarnishing can be allowed for as the main peak redshifts by 0.14 eV for all samples measured. The negative resonances present at higher energies undergo similar changes, with the negative shoulders of figure 6 disappearing after atmospheric exposure. Such shoulders have been attributed to quadrupolar resonances associated with sharp structures, which are then rounded away by tarnishing [24, 28].

The combination of RAS and low angle deposition hence provides a tool where the morphology can be tailored by the growth process and the optical behaviour monitored at the same time. Structures resonating at particular energies, as required for any enhancement spectroscopy, can be reliably obtained using this simple self-assembly technique. Figure 6(D) finally shows that the spectra depend on the initial template morphology, with a linear redshift of the positive peak with increasing template periodicity and a blueshift of the negative one. At resonance, a polarization of almost 50% of the total reflected light can be observed, confirming the strong dichroic response obtained with an Ag layer of average thickness of only 0.7 nm.

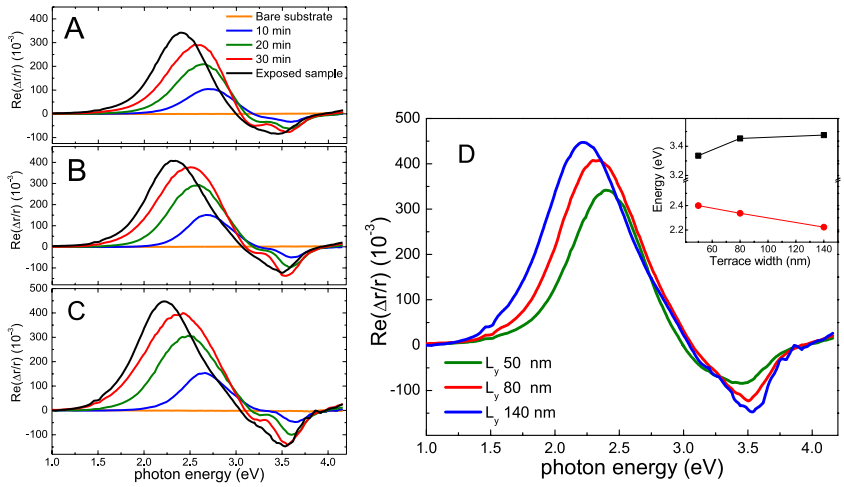

Figure 6. RAS spectra measured during growth interruptions and after exposure of the sample to the atmosphere for the 50 nm (A), 80 nm (B) and 140 nm (C). After exposure of the samples to the atmosphere modifications of the RAS spectra for different template periodicity l_y can be observed (D). (Inset) Energy position for the positive (circles) and negative (squares) peaks as a function of the periodicity l_y.

3. Theory and simulation

In order to compare theory and experimental results a three-layer model has been used [29], comprising an anisotropic layer containing the nanocomposite at the interface between two optically isotropic media. In the present case the transparent isotropic media are $Al_2O_3(0001)$ and air, with known dielectric functions ε_b [30] and $\varepsilon_{cap} = 1$, respectively. If the anisotropic layer has a thickness d much smaller than the exciting wavelength λ and an effective dielectric function $\bar{\varepsilon} = (\bar{\varepsilon}_x, \bar{\varepsilon}_y)$, the RAS response can then be written as [31]

$$\mathrm{Re}\left[\frac{\Delta r}{r}\right] = \frac{4\pi d}{\lambda}\mathrm{Im}\left[\frac{\bar{\varepsilon}_x - \bar{\varepsilon}_y}{\varepsilon_b - 1}\right]. \tag{2}$$

Using equation (2) it is possible to simulate the RAS spectra once the surface dielectric anisotropy (SDA) $d(\bar{\varepsilon}_x - \bar{\varepsilon}_y)$ is known. As the NP filling factor is 15% and the NP height is 13 nm an effective dielectric thickness $d \sim 1$ nm can be assumed for all the samples. For such thin films, as the substrate is transparent, the real RAS response is directly related to the imaginary part of $\bar{\varepsilon}$. For this reason, from the RAS it is possible to directly observe the plasmonic evolution of the NP layer with increasing thickness. RAS and the absorbance obtained from polarized transmission spectroscopy then provide equivalent information [21].

The anisotropic layer is modelled by metal NPs, all of the same ellipsoidal shape, size and orientation placed on top of the substrate in a rectangular lattice. Given the small dimensions of the particles involved, the quasistatic approximation will be assumed to hold. The effective dielectric function $\bar{\varepsilon}$ of a system of small identical ellipsoidal particles is

$$(\bar{\varepsilon} - \varepsilon_{cap})\mathbf{E}_{ext} = N\varepsilon_{cap}\alpha\mathbf{E}_{loc} \tag{3}$$

where N is the number of particles per unit area, $\mathbf{E}_{ext}$ is the macroscopic electromagnetic field, $\mathbf{E}_{loc}$ the local field and α is the polarizability of the isolated particle. In particular, the local field is the sum of $\mathbf{E}_{ext}$, of the image charges generated by the substrate $\mathbf{E}_{im}$ and of the electric field generated by the neighbouring particles $\mathbf{E}_{int}$. The local electric field can be expressed as

$$\mathbf{E}_{loc} = \frac{\mathbf{E}_{ext}}{1 + \alpha\beta} \tag{4}$$

where β is an interparticle interaction parameter. Substituting equation (4) into (3) leads to a polarization-dependent, in-plane effective dielectric function:

$$\bar{\varepsilon}_i = \varepsilon_{cap}\left(1 + \frac{N\alpha_i}{1 + \alpha_i\beta_i}\right) \tag{5}$$

where $i = (x, y)$, resulting in a dichroic signature from the nanocomposite layer. Using this model, the shifts in the resonance position upon increase of the deposited thickness observed in figure 6 can be explained by stronger NP coupling interactions due to increasing NP volume at fixed NP centre-to-centre distances, combined with larger aspect ratios of the single NPs.

In order to correctly model the observed optical characteristics, the dipolar approaches typically utilized for similar systems need to be modified. First, when RAS is measured *ex situ*, the effect of tarnishing of the NPs has also to be considered due to surface sulphurization of the Ag [32] and the normal expression for α [33] must be modified. It is assumed that the Ag core remains unchanged, but the outer layer of the NPs become an Ag_2S shell with the same aspect ratio. If s_x is the shell thickness along the x direction, ε_s is the dielectric function of the Ag_2S shell [32], $f_v = R_x^3/(R_x + s_x)^3$ is the volumetric fraction occupied by the core and V_p is the volume of the particle, then the polarizability of the isolated NP in SI units is [33, 28]

$$\begin{aligned}\alpha_i = V_p\{&(\varepsilon_s - \varepsilon_{cap})[\varepsilon_s + (\varepsilon_m - \varepsilon_s)(1 - f_v)L_i] \\ &+ f_v\varepsilon_s(\varepsilon_m - \varepsilon_s)\}\{[\varepsilon_s + (\varepsilon_m - \varepsilon_s)(1 - f_v)L_i] \\ &\times [\varepsilon_{cap} + (\varepsilon_s - \varepsilon_{cap})L_i] + f_vL_i\varepsilon_s(\varepsilon_m - \varepsilon_s)\}^{-1}.\end{aligned} \tag{6}$$

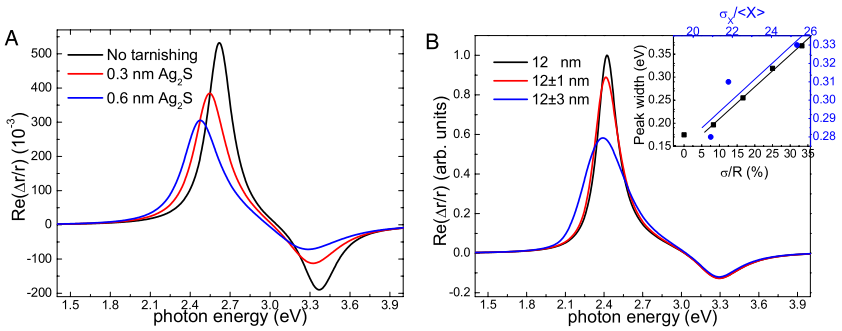

Figure 7. (A) Simulated RAS spectra for different tarnishing thickness with parameters listed in table 2. The peaks redshift and broaden when a dielectric shell is formed. (B) RAS spectra for interacting spheres in the monodispersed case with $R = 12$ nm and for a spherical ensemble with $R = 12 \pm 1$ nm and 12 ± 3 nm. Inset: theoretical (square) and experimental (circle) relation between the Gaussian width of the main peak and relative standard deviation, showing an almost linear trend.

In equation (6), L_i are the shape depolarization factors that take into account shape anisotropy of the isolated NP and ε_{m} is the dielectric function of Ag with a correction in its imaginary part in order to take into account the reduced relaxation time due to particle confinement [19]. The scattering rate is assumed to be $\Gamma_i = \Gamma_{\mathrm{b}} + A_i v_{\mathrm{f}}/R_i$, where Γ_{b} is the bulk scattering rate value, A_i is a constant of the order of unity, v_{f} is the Fermi velocity and R_i is the semiaxis of the NP in the i direction. Under the assumption that the collision processes are independent, the relaxation rates can be added according to Matthiessens' rule, so that a further increase in Γ_i due to polycrystallinity of the NPs can also be included. In the rest of the paper it will be assumed that $A_i = 0.5$.

The interaction parameter β also requires modification. The parameter is usually expressed as a dipole sum:

$$\beta = \frac{1}{4\pi}\left(F\sum_j \frac{3\cos^2\theta_j' - 1}{r_j'^3} + \sum_j \frac{3\cos^2\theta_j - 1}{r_j^3}\right) \qquad (7)$$

where $F = \frac{\varepsilon_b - \varepsilon_{\mathrm{cap}}}{\varepsilon_b + \varepsilon_{\mathrm{cap}}}$, θ_j is the dipole angle, θ_j' is the image dipole angle and the self-image is included in the summation. The distances of an ellipsoid from the jth dipole and the jth image charge are $\mathbf{r}_j$ and $\mathbf{r}_j'$, respectively. Equation (7) was already introduced by Yamaguchi in his pioneering work more than 30 years ago and it has been recently used to describe the behaviour of similar NP arrangements [34]. However, it was recently demonstrated [35] that this model predicts inaccurate results for supported flattened NPs. An analytical solution is available for NPs with rotational symmetry about the surface normal, where the contribution of the imaginary charges can be correctly estimated [36]. Following this approach, an effective distance for the NP from the substrate has been obtained in the present case by approximating the NPs as oblate spheroidal particles with average in-plane radius $\bar{R} = (R_x + R_y)/2$. In this way it was possible to correct the value of $\mathbf{r}_j'$ and of the β_i coefficient. The errors in the resonance position due to the assumed NP isotropy were estimated to be smaller than 0.02 eV.

With the modifications introduced for both α_i and β_i, the resonance condition in the effective dielectric function of the NP layer can be found at the poles of the imaginary part of equation (5). Figure 7(A) shows the RAS signal from ellipsoids with different coating thickness (parameters are listed in table 2). The spectra present the same double-peak feature of figure 6 and a comparable peak intensity. In particular, the peaks redshift and broaden when the outer layer of the metal core is replaced by a dielectric shell to simulate tarnishing. This behaviour is consistent with modifications of the dielectric environment surrounding the particles, from air to a dispersive material with higher refractive index, in our case Ag_2S. From figure 6 a main peak redshift of 0.14 eV was measured after exposure of the samples to the atmosphere, corresponding in our model to a thickness $s_x = 0.6$ nm. This approach could be further extended to monitor the chemical growth of a dielectric shell *in situ*, where the dielectric shell formed could produce a desired shift in the resonance position.

Table 2. Parameters used in the simulations shown in figures 7(A) and (B). The column refers respectively to the anisotropic NP arrays coated with different dielectric shell thickness and to interacting spherical arrays with radial dispersion but fixed interparticle separation.

	Ag_2S-coated	Dispersion
l_y (nm)	81	81
l_x (nm)	36	—[a]
R_y (nm)	10	12
R_x (nm)	14.5	12
R_z (nm)	7	12
s_x (nm)	0/0.3/0.6	

[a] The interparticle distance was defined as $l_x = 2R + 5$ nm and R was varied.

The model utilized here not only reproduces semi-quantitatively the lineshapes measured with RAS, but also provides information on the statistical properties of the ensemble. The morphological dispersion can be simulated convoluting the morphological Gaussian distributions with the $\mathrm{Re}[\Delta r/r]$ profiles obtained for the different morphological parameters. Generally speaking, if $\mathrm{Re}[\Delta r/r(X)]$ is a function of a random variable X, which follows a Gaussian distribution with average value $\langle X\rangle$ and standard deviation σ, we expect a broadening of the measured peaks. In this case the effective

RAS signal can be written as

$$\overline{\mathrm{Re}}\left[\frac{\Delta r}{r}\right] = \frac{1}{\sigma\sqrt{2\pi}} \times \int \mathrm{Re}\left[\frac{\Delta r}{r}(X)\right] \exp[-(X-\langle X\rangle)^2/2\sigma^2]\,\mathrm{d}X. \quad (8)$$

Where the spectra depend on other independent random variables the integral for each of them can be calculated independently due to linearity of the integral operator. As a representative example to clarify the effects of morphological distribution, we consider interacting spheres of average radius $R = 12$ nm with a fixed interparticle separation of 5 nm, similar to the experimental results. As the NP radius increases, the volume and thus the coupling along the arrays increases, producing a redshift of the main peak but leaving the negative peak almost unchanged. In order to show clearly the effect of peak broadening in the simulation, the NP interaction was increased by doubling the size of the β parameter. Figure 7 shows the modelled RAS spectra for monodispersed spheres and after Gaussian convolution with standard deviations of 1 and 3 nm (parameters are listed in table 2). In the presence of morphological dispersion, the RAS peaks appear broadened as expected. This is particularly evident for the positive peak, as it is the one most sensitive to changes in the interaction volume. The inset in figure 7(B) (black line) shows that the theory predicts a linear relationship between width and standard deviation. This is in accordance with the experiment (blue line), where samples showing the largest morphological dispersion (calculated by averaging all the relative from table 1) are associated with the broader peaks. RAS can then not only measure the resonance energy of tunable Ag NP arrays during growth, but it can also monitor the overall order of the surface through the Gaussian broadening of the main peak.

In order to finally reproduce the RAS spectra, the presence of the step needs to be taken into consideration. This can be done assuming that the NPs are surrounded by an effective homogeneous medium $\varepsilon_{\mathrm{eff}}$ being a simple weighted average of substrate and air, with f being the fractional weight:

$$\varepsilon_{\mathrm{eff}} = \varepsilon_b f + \varepsilon_{\mathrm{air}}(1-f). \quad (9)$$

With all these modifications, the dependence of the RAS spectra on the initial template periodicity has been modelled, as shown in figure 8. The in-plane morphology is taken from the SEM analysis of table 1, a tarnished layer with $s_x = 0.6$ nm is assumed for all the samples and $f = 0.25$ has been chosen from geometrical considerations. NP out-of-plane radii of 6 nm, 7 nm and 8 nm were used for the 50 nm, 81 nm and 140 nm periodicity, respectively. The trend in figure 8 resembles the one measured experimentally: the main peak redshifts and the negative one slightly blueshifts with increasing periodicity. This simple model produces semi-quantitative agreement with the experimental trends observed. However, quantitative fitting of the peak positions cannot be precisely obtained. The simulation parameters suggest that the shift between the in-plane resonances can be inferred to be an interplay between NP elongation along the array axis and the interparticle interaction, whose effects

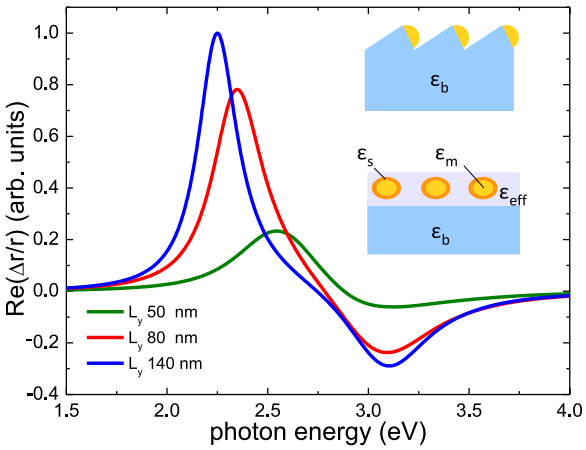

Figure 8. Simulated RAS spectra of Ag NP arrays with different periodicities l_y. In the inset a comparison between the real structure (top) and the simulated one (bottom) is presented. The spectra resemble the measured behaviour profile of figure 6(D).

are comparable in size. As they both affect the RAS spectra in similar ways, care will be required in developing more quantitative models of the optical response. However, this offers advantages for varying the optical properties of the arrays as the main peak position can be tuned over an even larger energy range (in the present case up to 0.6 eV, corresponding to more than 100 nm in the visible region of the spectrum), thus increasing the versatility of the glancing angle deposition technique. The model can be considered as an approximate guide for the factors governing the optical behaviour of NP arrays and it has been able to explain the features measured experimentally. The *in situ* optical monitoring, which RAS provides, will then allow the necessary refinements of growth and template parameters required to produce the desired resonant structure.

4. Conclusion

Stepped templates have been prepared by annealing α-Al_2O_3 in the atmosphere and it has been shown that the surface periodicity can be easily controlled by altering the annealing conditions. NP arrays with long range order and good uniformity over the entire substrates have been formed using glancing angle deposition. RAS has been used *in situ* to monitor the evolution of the optical dichroic response of the NP array with deposition time and the consequent increase in NP size. It has been shown that different substrate periodicities tailor different NP morphologies leading to consistent changes in the RAS properties of the array. In this way, tunability of the optical properties of the NP arrays over a wide energy range has been obtained. A model has been developed to provide a semi-quantitative explanation of the optical behaviour of the samples. The model is successful in explaining the effects of atmospheric exposure and morphological dispersion on the spectra. In particular, it was shown that RAS can not only provide information on the resonant energy of the anisotropic layer during the growth, but

also give an indication on the overall order via the Gaussian broadening of the main peak. While the simulations provide guidance regarding the physical origin of the large optical anisotropies observed in the experimental data, fine tuning of the resonant features is most readily obtained by using the *in situ* monitoring capability that RAS provides to form structures with engineered optical spectral features.

5. Methods

Single-crystal, single-side-polished α-Al_2O_3(0001) substrates, miscut 6° along the [1$\bar{2}$10], were used to obtain stepped templates. After a solvent treatment, the substrates were loaded in a high purity alumina crucible, inserted in an alumina tube furnace and annealed in the atmosphere at different temperatures above 1200 °C for 24 h in order to obtain an ordered terrace and stepped structure. The annealed templates were subsequently loaded into the HV growth chamber (base pressure 3×10^{-8} mbar) and the sample surface was aligned at the required grazing angle with respect to the Ag atom flux using an optical manipulator. The proximity of each surface and the large distance (70 cm) between the crucible and the samples ensure the same coverage for each of the deposited samples. The NPs were prepared by depositing Ag on the substrates at room temperature with a calibrated rate at normal incidence equivalent to 0.23 nm min^{-1}.

The RAS spectra were recorded *in situ* during growth interruptions, and also *ex situ*. The RAS spectrometer is home-built and follows the Aspnes photoelastic modulator design [37]. Measurements were performed over a broad spectral range, from 0.8 to 4.2 eV.

The in-plane morphology of the cluster layer was determined using an ULTRA SEM built by Carl Zeiss (Germany), while an FEI Titan TEM was used to obtain an out-of-plane cross section of the nanocomposite layer. TEM sections were prepared for both an annealed surface and an Ag-deposited sample. A 10 nm Au/Pd layer was deposited by sputtering in order to protect the nanocomposite layer. Subsequently, the sample was prepared for TEM analysis in a Carl Zeiss Auriga CrossBeam FIB-SEM. The *in situ* lift-out technique was used to remove a section of the sample and affix it to a TEM grid. The sample was then polished to ∼100 nm thickness with 30 keV gallium ions. In order to reduce surface damage and amorphization, the sample was finally polished with 5 keV gallium ions. Once prepared, the samples were imaged by the TEM, operating at 300 kV. The substrate was aligned to the [10$\bar{1}$0] zone axis for imaging. In all cases the images were acquired in bright-field mode.

Acknowledgments

We would like to thank R G S Sofin and N McAlinden for useful suggestions. Work funded by the Science Foundation of Ireland, contract no 06/IN.1/I91 under the framework of the INSPIRE programme, funded by the Irish Government's Programme for Research in Third Level Institutions, Cycle 4, National Development Plan 2007-2013

References

[1] Brongersma L M and Kik P G 2007 *Surface Plasmon Nanophotonics* (Berlin: Springer)
[2] Quinten M, Leitner A, Krenn J R and Aussenegg F R 1998 Electromagnetic energy transport via linear chains of silver nanoparticles *Opt. Lett.* **23** 1331–3
[3] Lamprecht B, Schider G, Lechner R T, Ditlbacher H, Krenn J R, Leitner A and Aussenegg F R 2000 Metal nanoparticle gratings: influence of dipolar particle interaction on the plasmon resonance *Phys. Rev. Lett.* **84** 4721–4
[4] Maier S, Kik P, Atwater A and Meltzer S 2003 Local detection of electromagnetic energy transport below the diffraction limit in metal nanoparticle plasmon waveguides *Nature Mater.* **2** 229–32
[5] Pellegrini G, Mattei G and Mazzoldi P 2009 Tunable, directional and wavelength selective plasmonic nanoantenna arrays *Nanotechnology* **20** 065201
[6] Polman A and Atawer H A 2010 Plasmonics for improved photovoltaic devices *Nature Mater.* **9** 205–13
[7] Nie S and Emory S R 1997 Probing single molecules and single nanoparticles by surface-enhanced Raman scattering *Science* **275** 1102–6
[8] Jain P K, Huang X and El-Sayed I H 2007 Review of some interesting surface plasmon resonance-enhanced properties of noble metal nanoparticles and their applications to biosystems *Plasmonics* **2** 107–18
[9] Halas N J, Lal S, Chang W-S, Link S and Nordlander P 2008 Plasmons in strongly coupled metallic nanostructures *Chem. Rev.* **37** 898–911
[10] Zou S and Schatz G C 2005 Silver nanoparticle array structures that produce giant enhancements in electromagnetic fields *Chem. Phys. Lett.* **403** 62–7
[11] Kim S, Jin J, Kim Y-J, Park I-Y, Kim Y and Kim S-W 2008 High-harmonic generation by resonant plasmon field enhancement *Nature* **453** 757–60
[12] Kinkhabwala A, Yu Z, Fan S, Avlasevich Y, Mullen K and Moerner W E 2009 Large single-molecule fluorescence enhancements produced by a bowtie nanoantenna *Nature Photon.* **3** 654–7
[13] Grigorenko A N, Roberts N W, Dickinson M R and Zhang Y 2008 Nanometric optical tweezers based on nanostructured substrates *Nature Photon.* **2** 365–70
[14] Jain P K and El-Sayed M A 2008 Noble metal nanoparticle pairs: effect of medium for enhanced nanosensing *Nano Lett.* **8** 4347–52
[15] Burda C, Chen X, Narayanan R and El-Sayed M A 2005 Chemistry and properties of nanocrystals of different shapes *Chem. Rev.* **105** 1025–102
[16] Maier S A, Brongersma M L, Kik P G and Atwater H A 2002 Observation of near-field coupling in metal nanoparticle chains using far-field polarization spectroscopy *Phys. Rev.* B **65** 193408
[17] Sugawara A, Hembree G and Scheinfein M R 1997 Self-organized mesoscopic magnetic structures *J. Appl. Phys.* **82** 5662–9
[18] Cuccureddu F, Murphy S, Shvets I V, Porcu M and Zandbergen H W 2008 Plasmon resonance in silver nanoparticles arrays grown by atomic terrace low-angle shadowing *Nano Lett.* **8** 3248–56
[19] Verre R, Fleischer K, Smith C, McAlinden N, McGilp J F and Shvets I V 2011 Probing the out-of-plane optical response of plasmonic nanostructures using spectroscopic ellipsometry *Phys. Rev.* B **84** 085440

[20] Evlyukhin A B, Bozhevolnyi S I, Stepanov A L and Krenn J R 2006 Splitting of a surface plasmon polariton beam by chains of nanoparticles *Appl. Phys.* B **84** 29–34
[21] Verre R, Fleischer K, Sofin R G S, McAlinden N, McGilp J F and Shvets I V 2011 *In situ* characterization of one-dimensional plasmonic Ag nanocluster arrays *Phys. Rev.* B **83** 125432
[22] Chan W L and Chason E 2007 Making waves: kinetic processes controlling surface evolution during low energy ion sputtering *J. Appl. Phys.* **101** 121301
[23] Oates T W H, Keller A, Noda S and Facsko S 2008 Self-organized metallic nanoparticle and nanowire arrays from ion-sputtered silicon templates *Appl. Phys. Lett.* **93** 063106
[24] Lazzari R, Roux S, Simonsen I, Jupille J, Bedeaux D and Vlieger J 2002 Multipolar plasmon resonances in supported silver particles: the case of Ag/α-Al_2O_3(0001) *Phys. Rev.* B **65** 235424
[25] Marnier A and Parker S C 2004 *Ab initio* morphology and surface thermodynamics of α-Al_2O_3 *Phys. Rev.* B **69** 115409
[26] Fort E, Ricolleau C and Sau-Pueyo J 2003 Dichroic thin films of silver nanoparticle chain arrays on facetted alumina templates *Nano Lett.* **3** 65–7
[27] Weightman P, Martin D S, Cole R J and Farrell T 2005 Reflection anisotropy spectroscopy *Rep. Prog. Phys.* **68** 1251–341
[28] Flores-Camacho J M, Sun L D, Saucedo-Zeni N, Weidlinger G, Hohage M and Zeppenfeld P 2008 Optical anisotropies of metal clusters supported on a birefringent substrate *Phys. Rev.* B **78** 075416
[29] McIntyre J D E and Aspnes D E 1971 Differential reflection spectroscopy of very thin surface films *Surf. Sci.* **24** 417–34
[30] Palik E D 1998 *Handbook of Optical Constants of Solids* vol 3 (Amsterdam: Elsevier)
[31] Aspnes D E and Studna A A 1985 Anisotropies in the above—band-gap optical spectra of cubic semiconductors *Phys. Rev. Lett.* **54** 1956–9
[32] Bennett J M, Stanford J L and Ashley E J 1970 Optical constants of silver sulfide tarnish films *J. Opt. Soc. Am.* **60** 224–32
[33] Bohren C F and Huffman D R 1983 *Absorption and Scattering of Light by Small Particles* (New York: Wiley)
[34] Camelio S, Babonneau D, Lantiat D, Simonot L and Pailloux F 2009 Anisotropic optical properties of silver nanoparticle arrays on rippled dielectric surfaces produced by low-energy ion erosion *Phys. Rev.* B **80** 155434
[35] Valamanesh M, Borensztein Y, Langlois C and Lacaze E 2011 Substrate effect on the plasmon resonance of supported flat silver nanoparticles *J. Chem. Phys.* C **115** 2914–22
[36] Bedeaux D and Vlieger J 2001 *Optical Properties of Surfaces* (London: Imperial College Press)
[37] Aspnes D E 1985 Above-bandgap optical anisotropies in cubic semiconductors: a visible-near ultraviolet probe of surfaces *J. Vac. Sci. Technol.* B **3** 1498–506